Temperature dependence of film rupture and internal structural stability in liquid aluminium alloy foams

F. García-Moreno[1,2], M. Jürgens[2], J. Banhart[1,2]

[1] Helmholtz Zentrum Berlin für Materialien und Energie, Hahn-Meitner-Platz 1, 14109 Berlin, Germany

[2] Technische Universität Berlin, Hardenbergstr. 36, 10623 Berlin, Germany

Abstract

The morphology of solid metallic foams is governed by the evolution of the cellular structure during the foaming process in the liquid state. We study quantitatively film ruptures in liquid aluminium alloy foams and determine their temperature dependence and spatial distribution and analyse how they evolve during isothermal holding. The coalescence rate of AlSi8Mg4 and AlSi9 foams was found to increase linearly with temperature within the range studied. We introduce the term "internal structural stability" and quantify it by using the total number of bubbles and the coalescence rate. Furthermore, a probabilistic approach allows us to fit and extrapolate the number of bubbles as a function of holding time and to predict foam half-lives. Application of the two methods allows us to compare two established foamable alloys and to conclude that the internal structure of liquid AlSi8Mg4 foams is around 50% more stable than of AlSi9 foams.

Key words: metal foam; film rupture; coalescence; X-ray; foam structural stability

1 Introduction

Metal foams are a special case of the more general class of cellular metals and are prepared by creating gas bubbles in a metal or alloy, letting them arrange to a liquid foam, and solidifying to obtain a solid foam [1]. The temperature and time interval the metal foam is kept in the liquid state during foaming influence the ensuing solid structure as the liquid foam ages and changes its morphology, e.g. by coalescence. Knowing what governs such changes is crucial for commercialization of metal foam production and application in areas such as light-weight construction, functional components and architecture and design [2]. In all these cases, the homogeneity of the foam structure is crucial since mechanical properties can be negatively affected by wide cell size distribution and collapsed or bent cell walls [3-5]. To produce metal foam casting or powder metallurgy is applicable [6]. The latter consists of preparing a

foamable precursor by mixing and compacting metal powders with a blowing agent and then melting and foaming the compacted alloy. When producing large metal foam components, the foam has to be kept partially or fully liquid for a period of time during which notable foam degradation by coalescence and drainage takes place. This work attempts to quantify such degradation processes and relate them to processing parameters. In such it builds on a previous study [7]. Note that some cellular metals are not foams in the sense defined here and are governed by different mechanisms not treated here.

The structure of a liquid foam depends on several factors such as alloy composition [8], method of precursor compaction [9-12], kinetics of blowing agent decomposition [13], number of nucleation sites [14] or liquid film stability [15, 16]. In foams produced by melt processing, stability is provided by the joint action of dispersed solid particles and oxide films [17-19], whereas in foams created by the powder metallurgical route oxides residing in the powders are crucial for stabilisation [16, 20, 21]. Up to now, the stability of metal foams has been studied by observing their collapse during isothermal holding before solidification [22-24] or by post-mortem analysis of foam morphology after solidification [16, 25, 26]. The terms "bubble" and "pore" represent the same structural part of a foam, namely a closed cell, but in the liquid and solid state, respectively.

The simplest measure for foam stability is the maximum height a growing foam column can reach [1, 27]. This consideration is similar to what Brady et al. [28] and Bikerman [29] proposed for aqueous foams, where additionally the lifetime (also known as collapse time) of a foam in a column or the time interval after which the foam column has decayed to half its maximum height is used to describe foam stability [28, 30]. Another option is to consider the relationship between maximum foam expansion and foam collapse i.e. the ratio between the foam volume at maximum expansion and that after a certain holding period. Such macroscopic values can be easily measured and reflect the macroscopic stability of a foam. However, they do not characterise directly the internal structural stability of a foam and are, for example, influenced by the oxidation of the outer foam skin [31]. This is why we need to consider two different types of stabilities, namely i) macroscopic or external stability and ii) internal structural stability.

In any liquid foam, a lack of film stability leads to bubble coalescence, which gives rise to a topological rearrangement of the structure [32, 33]. Other topological changes occur during foam evolution, for example coarsening by gas interdiffusion promoted by a difference in gas pressure between adjacent bubbles of different diameters [34], or by an active gas source such

as a blowing agent particle [35]. Other factors including the effective viscosity of the liquid [36, 37], film surface tension [37], film thinning due to drainage [34, 38] or liquid flow caused by gravitational drainage [26, 39-42] also have to be taken into account. The latter effect was found to be of minor importance in microgravity experiments [43]. Especially in metal foams, other parameters such as the surrounding gas atmosphere or pressure [44], the heating rate [45] and the holding time and end temperature in the liquid state [7] influence the kinetics of the internal structure and external volume evolution. Film rupture and the ensuing coalescence are fast as revealed by X-ray radioscopy [46]. A statistical observation of this phenomenon yielded a clear time and temperature dependence of the rate of coalescence [7].

In this work, we use in-situ X-ray radioscopy and X-ray tomography to analyse the time and temperature dependence of coalescence in liquid metal foams quantitatively. We present a criterion for foam stability based on the measurement of the corresponding film rupture density rate, i.e. the number of ruptures in a defined volume and time interval. Furthermore, we predict the bubble number evolution for the whole liquid foam life by assuming an exponential decay of pore numbers.

2 Experimental

2.1 Materials

Foamable precursors of alloys AlSi9 and AlSi8Mg4 (in wt.%), both containing 0.5 wt.% TiH_2 as a blowing agent, were produced by densifying powders. Elemental powders of Al (*ALPOCO Ltd.*), Si (*Alchem Ltd.*), AlMg50 (*Possehl Erzkontor GmbH*) and TiH_2 (*Chemetall GmbH*) were mixed for 15 min and cold compacted for 5 min at 300 MPa in a first step. In a second step, they were further compacted either uni-axially (for AlSi9, 15 min at 300 MPa) or by extrusion (for AlSi8Mg4 at 600 MPa), both at 350 °C. Cuboid precursor samples of 19.8 mm × 9.8 mm cross section and 6 mm height (the latter parallel to the foaming direction) amounting to a precursor volume of $V_P \approx 1.16$ cm^3 were prepared for foaming. As we carried out 5 experiments at each of the 7 holding temperatures, in total 70 samples were processed for the 2 alloys studied.

2.2 Furnace

For each foaming experiment, a piece of foamable precursor was placed inside a rectangular boron nitride (BN) crucible of inner dimensions $V_c = 20$ mm × 10 mm × 20 mm, around

which a Pt heating wire is coiled (see Fig. 1). The crucible is suspended in a steel frame at 8 small fixing points, thus creating an air gap and reducing undesired thermal flow. The crucible is further insulated by 30 mm of pressed alumina wool. The front and back windows along the path of the X-ray beam are kept free of the alumina insulation to avoid beam attenuation. The crucible is closed by a 2 mm-thick BN plate and 25 μm-thick Ti foils acting as a thermal radiation shield on the front and back windows. In addition, 0.3 mm-thick Al foil and 17 μm-thick Al foil as outer window are placed between the Ti foil and the outer openings. The spatial temperature distribution and temporal stability in the crucible at the foaming temperature are both ±1 K. The furnace was originally designed and built by the Swedish Space Corporation to be used for microgravity experiments and is described in further detail in the literature [40, 47].

2.3 X-ray radioscopy

The experiments consisted in foaming precursors in the BN crucible while continuously observing the development of the structure in real-time by X-ray radioscopy, as described in detail previously [40]. The X-ray setup is composed of a micro-focus X-ray source and a flat panel detector, both from *Hamamatsu*, Japan. Spatial resolution is given by the geometrical magnification of the divergent beam which was set to a factor of 4, thus projecting areas of 12.5 μm size onto each 50 μm-large detector pixel. Radiographic images of the samples were recorded in-situ by the detector once every second.

Foaming was performed by heating precursor specimens in the crucible to the foaming temperature at a rate of 2 K/s (see Video 1). These temperatures were chosen based on previous optimization procedures of foam expansion and final foam volume, resulting in the selection of 635 °C for AlSi9 and 630 °C for AlSi8Mg4. From the X-ray images, the foam volume expansion curve can be obtained as shown exemplary for the AlSi9 alloy in Fig. 2. Several foaming steps such as first local expansion after ~320 s, complete melting of the sample after ~345 s and a final expansion step after ~370 s until filling the whole crucible can be identified. Due to the constraint of the crucible the maximal achievable foam volume V_f is limited to $V_f = V_c \approx 4$ cm^3, corresponding to a maximal expansion ratio of $V_f/V_P \approx 3.4$. At this stage, the relative foam density is $\rho_f/\rho_p \approx 0.3$ (ρ_f *and* ρ_p are the absolute densities of the foam and the precursor material, respectively). Once a foam had fully filled the crucible and the temperature of the system had equilibrated during another 120 s, the isothermal holding temperature for a given experiment was adjusted after further 60 s and kept constant for the

next 600 s as illustrated in Fig. 3. Film rupture analysis began at $t = 500$ s (after beginning the experiment) or $t_0' = 0$ s on an adjusted time scale and ended at $t = 1100$ s or $t_f' = 600$ s. An analysis was performed for 5 repeated individual experiments for each parameter set (holding temperature, alloy). The holding time was limited to 600 s because for even longer times foam collapse and shrinkage frequently set in hindering comparisons. This procedure is shown exemplary for the AlSi8Mg4 alloy in Fig. 3. Cooling of the samples was done by simply switching off the heating power.

Bubble coalescence analysis is performed by counting the number of film ruptures n. This implies the assumption that a single film rupture corresponds to the coalescence of two, but not more, bubbles to one. The analysis was made by a pairwise comparison of subsequent X-ray radioscopic images by our own automatized software *Axim* [7]. Differences detected between images are related to film rupture events. Considering the effective pixel size of the imaging setup of 12.5 µm and the spatial resolution of the rupture detection software we chose a threshold of clusters of at least 20 pixels for rupture detection. This corresponds to a length scale of ~250 µm, below which bubbles are considered microporosity [48-50] and are excluded because their coalescence is difficult to detect and might not have a big influence on the final structure of resulting solid foams. Coalescence in the remaining bubbles can be detected reliably as proven by comparison of automatized with manual analyses of video sequences (see Video 2). The 20-pixel threshold also avoids artefacts produced by noise, intensity fluctuations or slight bubble movements from one frame to the next.

2.4 X-ray tomography

To verify the number of coalescence events derived from in-situ radioscopy, X-ray tomography on solidified samples foamed at selected temperatures was applied using the equipment used for radioscopy after substituting the foaming furnace by a rotation stage from *Huber,* Germany. 1300 projections of each sample were recorded while rotating by an angle of 360°. These projections were reconstructed to a 3D volume with an underlying voxel size of 12.5 µm with software *Octopus* and analysed quantitatively with software *Mavi*. As a result, the number of pores, their size distribution and their corresponding volumes were obtained. Three tomograms at t_0' and one at t_f' for three different holding temperatures were recorded for each alloy (i.e. in total 12 tomograms). For a quantification and comparison of the number of cells we applied a similar criterion as for radioscopy and discarded all pores

with an equivalent diameter ≤250 µm. The equivalent diameter was calculated from the volume of the pores obtained by tomography assuming a spherical pore shape.

To explore coalescence quantitatively, experiments were performed following the protocol described in Fig. 3 with the difference that the samples were solidified before ($t_0' = 0$ s) and after ($t_f' = 600$ s) holding period at a given temperature. The coalescence rate then follows from the reduction of pore number N during the holding period:

$$\frac{\Delta N}{t_f'} = \frac{N(t_0') - N(t_f')}{t_f'}. \tag{1}$$

This rate expresses how pores disappear during holding assuming that coarsening due to gas diffusion is negligible as it is a much slower process and no new pores are nucleated [51].

3 Results

3.1 Foam structure evolution

Fig. 4 shows representative radiographies of AlSi9 foams at t_0', $t_f'/2$ and t_f' for different temperatures. Qualitatively we can observe that the foam fills the crucible from t_0' until t_f' at every temperature. No collapse occurs and therefore $V_f(t_0') = V_f(t_f') = V_c$. Bubble diameters range from 1 mm to 8 mm with a slightly larger bubble size at the top of the foams. The structure visibly coarsens by coalescence during holding. After holding at t_f', bubbles appear slightly larger for the higher temperatures.

Fig. 5 shows the corresponding representative radiographies for AlSi8Mg4 foams in analogy to Fig. 4. We observe good filling of the crucible by foam and a stable foam volume for all conditions studied. Compared to AlSi9 the foam structure is finer, with smaller bubbles already at t_0'. And again, larger bubble diameters for longer holding times as well as for higher temperatures can be observed.

Although the foam structure appears predominantly uniform, X-ray radioscopy allows one to identify occasional inhomogeneities such as localised drainage effects at t_f' with slightly denser regions at the bottom, especially discernible for AlSi8Mg4 (Fig. 5).

3.2 Spatial distribution of film ruptures

The coordinates of the y-projections (X-ray beam direction) of all the liquid film rupture events detected in 5 individual experiments on AlSi9 foams are plotted as 2D rupture maps in Fig. 6 where each dot represents a single rupture event (at an unspecified time). Such maps allow for assessing the spatial distribution of film ruptures during the entire period of isothermal holding (600 s). The distributions of rupture events appear predominantly uniform to visual inspection, however, with some exceptions: i) a narrow border region of reduced rupture activity followed by ii) a second border region of increased activity, especially visible at the upper right for 620 °C and 640 °C, and iii) a region with low number of ruptures at the bottom and higher at the top of all samples as marked with blue and red ellipses. The total number of ruptures increases continuously with holding temperature.

The analogous analysis for AlSi8Mg4 is presented in Fig. 7. Again, mostly uniform rupture distributions with similar exceptions can be observed. The border effect with increased numbers of ruptures at all the borders, especially at the bottom, is more clearly visible than for AlSi9, especially for high temperatures. The number of ruptures is always higher for AlSi8Mg4 than for AlSi9 and also increases continuously with holding temperature.

3.3 Time dependence of film ruptures

The accumulated total number of ruptures $n(t)$ at a given time (i.e. summed up over the entire foam volume and over all 5 samples) for samples kept at various holding temperatures is displayed in Fig. 8 for both alloys. The number of ruptures increases with holding time for both alloys. The rupture rate is defined as $\dot{n} = dn/dt$ and was considered as largely constant for most experiments (large amount of bubbles and short measurement times) in a first approach [7]. Accordingly to $\dot{n}$ the first derivative of the rupture rate is $\ddot{n} = d^2n/dt^2$. But for AlSi9, $\ddot{n}$, i.e. the curvature of the curve, is positive (Fig. 8a), and negative for AlSi8Mg4 (Fig. 8b), especially for the first 300 s and low holding temperatures. For AlSi9 foamed at lower temperatures (580−610 °C), the slope ($\dot{n}$) is smaller during the first 120 s but then becomes similar to the one of the 580−600 °C curves. For both alloys, the higher the holding temperature, the higher the number of ruptures as already observed in Fig. 6 and Fig. 7.

3.4 Number of pores

Fig. 9 shows 2D slices extracted from 3D data sets of AlSi9 foams solidified before and after holding at different temperatures. The samples solidified before holding (at t_0') contain $N_{0,AlSi9} = 1401 \pm 64$ and $N_{0,AlSi8Mg4} = 2995 \pm 138$ pores larger than 250 µm (SD refers to the 3 samples investigated). The corresponding pore numbers after holding (only 1 sample) are also obtained and the difference to the pore number before holding given in Fig. 10. This difference ΔN represents the pores that have disappeared during holding and is compared to the number of films that have ruptured during holding as obtained by radioscopy, see Fig. 8. As the latter data has been summed up over 5 samples the numbers taken from Fig. 8 are divided by 5 to yield $\bar{n}$. ΔN increases with temperature and so does $\bar{n}$. The two values differ by less than 25 %.

4 Discussion

We chose in-situ X-ray measurements of film ruptures as an efficient way to determine coalescence. We assume that each single film rupture detected corresponds to a single coalescence event of two bubbles into one and neglect alternative scenarios such as: i) more than two bubbles merge after an almost simultaneous rupture of several directly neighbouring films, ii) several bubbles separated from each other in space merge independently in a time interval smaller than the temporal resolution (1 s) but overlap in the viewing direction and therefore are counted as one event, and iii) rupture avalanches in the neighbourhood of an initial rupture are triggered by the corresponding rearrangement of liquid but remain unnoticed due to limited time resolution.

Scenario i) appears unlikely as such simultaneous ruptures have never been observed even at image acquisition rates up to 10^5 Hz [52]. Scenario ii) is possible to a certain extent. However, looking at Fig. 6 and Fig. 7 and considering that all the roughly 3000 events depicted in each panel were created in 600 time steps in 5 samples, one can conclude that on average only one rupture is detected in one single foam in each time step and the chance that a second one is right in the line of sight of the first is negligible. Scenario iii) is well known for aqueous foams [53, 54] and rupture avalanches were recently found in liquid metal foams too [55], but they are quite rare and require a big triggering rupture event to be followed by a number of smaller ruptures mostly involving bubbles smaller than 250 µm not counted here. Therefore above basic assumption can be expected to be valid.

4.1 Spatial distribution of ruptures

The film ruptures observed for both alloys as shown in Fig. 6 and Fig. 7 are well distributed except for some regions featuring more rupture events. The foam structures of both alloys at t_0' (starting structure) as well after t_f' (aged structure) appear uniform, see Fig. 4 and Fig. 5, except for some larger bubbles and regions of low local foam densities at the top of the samples, especially at the end of the holding period (see blue ellipses in Fig. 4 and Fig. 5). Especially for AlSi9, these regions correlate with regions featuring more ruptures (see blue ellipses in Fig. 6 and Fig. 7). On the other hand, at the bottom of the foams fewer ruptures occur, which correlates with some notably denser regions (see red ellipses in Fig. 4, Fig. 5, Fig. 6 and Fig. 7) caused by the accumulation of liquid due to gravity-induced drainage [40, 56]. However, this effect has been shown not to be the most important one for foam stability [43]. Altogether, the redistribution of liquid due to gravity influences not only the foam density distribution but also the number of ruptures and accordingly the bubble size distribution. Furthermore this effect is more pronounced the higher the holding temperature is as previously shown [7].

There is one region with a significantly reduced number of ruptures at the bottom of the AlSi9 foam produced at 580 °C. This can be attributed to a foaming temperature too close to the eutectic temperature (577 °C), thus giving rise to a locally high melt viscosity or even to partially solid regions which hinder rupture as the precursors are made from elemental powders, which may still not have dissolved to form a homogeneous alloy. For the AlSi8Mg4 alloy with a eutectic temperature of 558 °C, which is markedly below the lowest holding temperature of 580 °C, this effect is not observed. It also differs from AlSi9 in that a larger amount of liquid phase is present at low holding temperatures [57].

We observed two border effects, i) first almost no ruptures, ii) then more ruptures going from the crucible walls towards the interior of the foam, see Fig. 7. The first effect is related to the arrangement of the bubbles in the constraining crucible, leading to a lower local density and fewer cell walls that could rupture [52]. The second effect is most pronounced for AlSi8Mg4 at 620 °C and 640 °C holding temperature. These regions after the first layer of bubbles which are in direct contact with the crucible walls made of hexagonal boron nitride of a high thermal conductivity of up to ~600 W/(m·K) [58], through which heat easily flows into the sample. On the other hand, the thermal conductivity of the foam can be ~1.5 orders of magnitude

lower (~30 W/(m·K)) as estimated for a similar alloy and foam with $\rho_f/\rho_p \approx 0.3$ [59]. Effect ii) can therefore be attributed to a higher local temperature at the liquid foam borders as the number of ruptures was found to be temperature dependent [7].

4.2 Temperature dependence of the rupture density rate

A clear relationship between the number of ruptures and the isothermal holding temperature was found for both alloys. In the temperature range studied, an increase in the number of ruptures of 141% and 90% was found for AlSi9 and AlSi8Mg4, respectively.

To characterize the structural stability of liquid metallic foams independently of the sample size we quantify the number n_d of ruptures in a fixed foam volume (in our case V_f) as a function of time and temperature and define the rupture density rate $\dot{n}_d$:

$$\dot{n}_d(t,T) = \frac{1}{V_f}\frac{dn(t,T)}{dt}, \tag{2}$$

which is given for AlSi9 and AlSi8Mg4 in Fig. 11, with $V_f \approx 4$ cm^3 and $dt = t_f' = 600$ s. A simple linear fit describes the temperature dependence in the range studied:

$$\dot{n}_d(t,T) = aT + b, \tag{3}$$

with values for a and b given in Fig. 11. The similar slope for both alloys suggests that various types of Al-based metal foams with differing compositions may behave in this way. We previously found a higher slope of $a = 0.015$ 1/K·cm·s for AlSi9, but for higher temperatures, a less accurately controlled environment (temperature gradients up to 45 K within a sample) and analysing without a size threshold for the bubbles [7].

Reasons for the temperature dependence of film rupture include, i) the temperature dependence of melt viscosity, or ii) the pressure differences created by the temperature dependent decomposition profile of the blowing agent [7, 60]. The viscosity η is known to follow an Arrhenius-Andrade dependence [61]:

$$\eta \sim e^{(1/T)}, \tag{4}$$

and hydrogen release rate from TiH$_2$ speeds up markedly from 600 °C to 650 °C [60]. Both effects support more ruptures.

4.3 Time dependence of ruptures

A notably reduced number of ruptures in the liquid AlSi9 foam is observed during the first 120−180 s of holding at 580 °C and 590 °C (see Fig. 8a). Even for 600 °C and 610 °C, the increase of the number of ruptures over time is initially lower. This is not the case for AlSi8Mg4 (see Fig. 8b), which supports the assumption made in the previous paragraph that the temperature in the foam is locally too close to the eutectic point of AlSi9. The temperature just equalises after several minutes over the whole sample and the rupture numbers then increase approximately linearly. At a closer look, the derivative of the rupture rate itself seems to be slightly positive for AlSi9 but negative for AlSi8Mg4 foams, in variation to the previous assumption of a linear increase of $n(t)$ [7]. An increase of the rupture rate in time for both alloys can be explained by the action of gravity-induced drainage. A possible reason for the negative curvature of the dependence for AlSi8Mg4 could be the Mg content, since Mg is easily oxidised, which gives a foam additional stability [19, 31, 62].

Obviously, the rupture rate cannot stay constant indefinitely as the number of bubbles is limited and coalescence has to level off. Therefore, a linear representation of the number of ruptures as suggested in Ref. [7] is an approximation valid only as long as the accumulated number of ruptures is still smaller than the total number of bubbles. In order to predict the whole time evolution of the number of bubbles we refer to a probabilistic expectation based on an exponential decay for $N(t)$:

$$N(t) = N_0 e^{-\lambda t}, \tag{5}$$

with $N_{0,AlSi9} = 1401 \pm 64$ and $N_{0,AlSi8Mg4} = 2995 \pm 138$ taken from Sec. 3.4. The time constant λ is determined by a one-parameter fit of the bubble number $N(t) = N_0 - n(t)/5$, with $n(t)$ taken from Fig. 8 summed over 5 single experiments. The result shown in Fig. 12 indicates a faster decay of $N(t)$ for AlSi9.

4.4 Structural foam stability

Fig. 11 shows that the film rupture density rate $\dot{n}_d$ is lower for AlSi9 than for AlSi8Mg4 at all temperatures, but this does not automatically mean that the former foam internal structure is more stable than the latter. The probability of film rupture also depends on the absolute number of films (or bubbles) in a given volume, which is why we define the internal structural stability $S_{int}(T)$:

$$S_{int}(T) = \frac{\bar{N}_0}{\dot{n}_d(T)}, \tag{6}$$

with $\bar{N}_0 = N_0/V_F$ (the number of bubbles in a defined volume of a foam at t_0') and with Eq. (2) obtain

$$S_{int}(T) = \frac{N_0 \, dt}{dn} = \frac{1}{p}, \tag{7}$$

with p the probability of coalescence of two bubbles in a time interval. The internal structural stability corresponds to the time that takes between two film ruptures in a defined foam volume. Values for all these quantities are given in Tab. 1. Comparing our two alloys, we conclude that AlSi8Mg4 exhibits ~51±5 % more internal structural stability than AlSi9. This value does not include any information about the shape of the pores, their size or distribution.

Another possibility to quantify internal structural stability is by comparing foam lifetimes. We obtain the half-life of foams by plotting $ln\,N(t)$ over time (see Fig. 12) and fitting the curves according to Eq. (5) by a straight line, slope λ, related to the half-life of the foams $t_{1/2}$ by:

$$t_{1/2}(T) = \frac{ln2}{\lambda}, \tag{8}$$

and presented in Fig. 13. For both alloys, half-life decreases with temperature, with AlSi8Mg4 having a ~47±5% longer half-life in agreement with above analysis. The decay in Fig. 13 is smoother for AlSi8Mg4 than for AlSi9, reflecting a better fit to Eq. (5) of the first alloy. This can be also observed in Fig. 12, leading to the conclusion that for AlSi9 other less probabilistic factors may play a more important role.

4.5 Radioscopy vs. tomography

The evolution of pore numbers as obtained from X-ray radioscopies in liquid foams is corroborated by X-ray tomographies of selected solid samples, see Fig. 10. Quantitative analyses of the number of pores by tomography are accurate, but several factors have to be considered: i) the foams analysed by tomography before and after holding are obviously not the same, just different foams made under the same conditions, ii) the solidification process may introduce some changes to the structure. Factor i) can be mitigated by using exactly the same foaming conditions and several samples to improve statistics. ii) Solidification effects

are more pronounced when cooling slower than under the faster natural cooling conditions applied here [63].

In-situ time-resolved X-ray tomography would be the best method to analyse the morphological evolution and therefore foam stability [35, 64]. Such methods have become available recently [35] and could be used in the future to characterise bubble coalescence directly once large enough samples can be studied.

5 Conclusions

Aluminium alloys were converted to liquid foam and the evolution of their structure studied in-situ by means of X-ray radioscopy. The objective was to characterise film rupture events that lead to bubble coalescence and to establish the phenomena as a function of foam holding temperature and alloy. A quantitative analysis was carried out. Compared to earlier studies, a high number of samples (70) was processed for the sake of statistical certainty, the temperature was controlled within ± 1 K, two common alloys were compared and X-ray tomography was used to verify radioscopy.

The following main conclusions were derived:

- The spatial distribution of film ruptures in a liquid metal foam is uniform except for boundary effects related to the bubble density and heat transfer between foam and crucible. At elevated temperatures, the upper foam regions show more ruptures due to gravity-induced drainage.

- The coalescence rate of AlSi8Mg4 and AlSi9 foams increases approximately linearly with temperature within the studied range from 580 °C to 640 °C.

- Assuming an exponential decay of the number of bubbles we obtain foam half-lives in the range from 1000 to 3000 s, longer in AlSi8Mg4 than in AlSi9 and longest for the lowest temperature.

- Structural foam stability can be defined quantitatively in terms of a parameter S and is 50% higher for AlSi8Mg4 than for AlSi9 alloy.

6 Acknowledgements

7 References

[1]   J. Banhart, Metal foams: Production and stability, Adv. Eng. Mater. 8 (2006) 781-794.
[2]   F. García-Moreno, Commercial applications of metal foams: Their properties and production, Materials 9 (2016) 85.
[3]   E. Andrews, W. Sanders, L. J. Gibson, Compressive and tensile behaviour of aluminum foams, Mater. Sci. Eng., A 270 (1999) 113-124.
[4]   J. L. Grenestedt, On interactions between imperfections in cellular solids, J. Mater. Sci. 40 (2005) 5853-5857.
[5]   U. Ramamurty, A. Paul, Variability in mechanical properties of a metal foam, Acta Mater. 52 (2004) 869-876.
[6]   J. Banhart, Manufacture, characterisation and application of cellular metals and metal foams, Prog. Mater. Sci. 46 (2001) 559-632.
[7]   F. Garcia-Moreno, E. Solorzano, J. Banhart, Kinetics of coalescence in liquid aluminium foams, Soft Matter 7 (2011) 9216-9223.
[8]   H. M. Helwig, F. Garcia-Moreno, J. Banhart, A study of Mg and Cu additions on the foaming behaviour of Al-Si alloys, J. Mater. Sci. 46 (2011) 5227-5236.
[9]   M. Nosko, F. Simančík, R. Florek, Reproducibility of aluminum foam properties: Effect of precursor distribution on the structural anisotropy and the collapse stress and its dispersion, Materials Science and Engineering: A 527 (2010) 5900-5908.
[10]   A. R. Kennedy, S. Asavavisithchai, Foaming of compacted Al-TiH$_2$ powder mixtures, in: Gregson PJ, Harris SJ (Eds.), Aluminum Alloys 2002: Their Physical and Mechanical Properties Pts 1-3, 2002, p.p. 251-256.
[11]   M. A. Rodriguez-Perez, E. Solorzano, J. A. De Saja, F. Garcia-Moreno, The time-uncoupled Aluminium free-expansion: Intrinsic anisotropy by foaming under conventional conditions, in: Lefebvre LP, Banhart J, Dunand DC (Eds.), Porous Metals and Metallic Foams: Metfoam, Montreal, Canada, DEStech, 2007, p.p. 75-78.
[12]   H. M. Helwig, S. Hiller, F. Garcia-Moreno, J. Banhart, Influence of compaction conditions on the foamability of AlSi8Mg4 alloy, Metall. Mater. Trans. B 40 (2009) 755-767.
[13]   C. Jiménez, F. Garcia-Moreno, B. Pfretzschner, P. H. Kamm, T. R. Neu, M. Klaus, C. Genzel, A. Hilger, I. Manke, J. Banhart, Metal foaming studied in situ by energy dispersive X-ray diffraction of synchrotron radiation, X-ray radioscopy, and optical expandometry, Adv. Eng. Mater. 15 (2013) 141-148.
[14]   J. Hartmann, A. Trepper, C. Körner, Aluminum integral foams with near-microcellular structure, Adv. Eng. Mater. 13 (2011) 1050-1055.
[15]   C. Körner, Foam formation mechanisms in particle suspensions applied to metal foams, Mater. Sci. Eng., A 495 (2008) 227-235.
[16]   C. Körner, M. Arnold, R. F. Singer, Metal foam stabilization by oxide network particles, Mater. Sci. Eng., A 396 (2005) 28-40.
[17]   V. Gergely, R. L. Jones, T. W. Clyne, The effect of capillarity-driven melt flow and size of particles in cell faces on metal foam structure evolution, Transactions of JWRI 30 (2001) 371-376.
[18]   G. Kaptay, Interfacial criteria for stabilization of liquid foams by solid particles, Colloids Surf., A 230 (2004) 67-80.
[19]   K. Heim, G. S. Vinod-Kumar, F. García-Moreno, A. Rack, J. Banhart, Stabilisation of aluminium foams and films by the joint action of dispersed particles and oxide films, Acta Mater. 99 (2015) 313-324.
[20]   A. Dudka, F. Garcia-Moreno, N. Wanderka, J. Banhart, Structure and distribution of oxides in aluminium foam, Acta Mater. 56 (2008) 3990-4001.

[21]   S. Asavavisithchai, A. R. Kennedy, In-Situ Oxide Stabilization Development of Aluminum Foams in Powder Metallurgical Route, High Temp. Mater. Processes 30 (2011) 113-120.

[22]   S. Asavavisithchai, A. R. Kennedy, The effect of Mg addition on the stability of Al-Al_2O_3 foams made by a powder metallurgy route, Scripta Mater. 54 (2006) 1331-1334.

[23]   S. Asavavisithchai, A. R. Kennedy, The role of oxidation during compaction on the expansion and stability of a foams made via a PM route, Adv. Eng. Mater. 8 (2006) 568-572.

[24]   D. Lehmhus, Dynamic collapse mechanisms in metal foam expansion, Adv. Eng. Mater. 12 (2010) 465-471.

[25]   S. W. Ip, Y. Wang, J. M. Toguri, Aluminum foam stabilization by solid particles, Can. Metall. Q. 38 (1999) 81-92.

[26]   V. Gergely, T. W. Clyne, Drainage in standing liquid metal foams: modelling and experimental observations, Acta Mater. 52 (2004) 3047-3058.

[27]   S. Asavavisithchai, A. R. Kennedy, Effect of powder oxide content on the expansion and stability of PM-route Al foams, J. Colloid Interface Sci. 297 (2006) 715-723.

[28]   A. P. Brady, S. Ross, The measurement of foam stability, J. Am. Chem. Soc. 66 (1944) 1348-1356.

[29]   J. J. Bikerman, Foams, Springer Berlin Heidelberg, 2013.

[30]   K. Malysa, K. Lunkenheimer, Foams under dynamic conditions, Curr. Opin. Colloid Interface Sci. 13 (2008) 150-162.

[31]   F. Simancik, K. Behulova, L. Bors, Effect of ambient atmosphere on the foam expansion, in: Banhart J, Ashby MF, Fleck NA (Eds.), Cellular Metals and Metal Foaming Technology: Metfoam, Bremen, MIT Publishing, 2001, p.p. 89-92.

[32]   D. Weaire, S. Hutzler, The Physics of Foams, Oxford University Press, Oxford, USA, 1999.

[33]   I. Cantat, S. Cohen-Addad, F. Elias, F. Graner, R. Höhler, O. Pitois, F. Rouyer, A. Saint-Jalmes, Foams: Structure and Dynamics, Oxford University Press, Berlin, Paris, New York, 2013.

[34]   S. Hilgenfeldt, S. A. Koehler, H. A. Stone, Dynamics of coarsening foams: Accelerated and self-limiting Drainage, Phys. Rev. Lett. 86 (2001) 4704-4707.

[35]   F. García-Moreno, P. H. Kamm, T. R. Neu, F. Bülk, R. Mokso, C. M. Schlepütz, M. Stampanoni, J. Banhart, Using X-ray tomoscopy to explore the dynamics of foaming metal, Nature Communications 10 (2019) 3762.

[36]   C. C. Yang, H. Nakae, The effects of viscosity and cooling conditions on the foamability of aluminum alloy, J. Mater. Process. Technol. 141 (2003) 202-206.

[37]   B. Y. Hur, S. H. Park, A. Hiroshi, Viscosity and surface tension of Al and effects of additional element, in: Kim HS, Park SY, Lee SW (Eds.), Eco-Materials Processing & Design, 2003, p.p. 51-56.

[38]   D. T. Wasan, A. D. Nikolov, L. A. Lobo, K. Koczo, D. A. Edwards, Foams, thin films and surface rheological properties, Prog. Surf. Sci. 39 (1992) 119-154.

[39]   N. Vandewalle, H. Caps, G. Delon, A. Saint-Jalmes, E. Rio, L. Saulnier, M. Adler, A. L. Biance, O. Pitois, S. Cohen Addad, R. Hohler, D. Weaire, S. Hutzler, D. Langevin, Foam stability in microgravity, J. Phys. Conf. Ser. 327 (2011) 012024.

[40]   F. Garcia-Moreno, S. T. Tobin, M. Mukherjee, C. Jimenez, E. Solorzano, G. S. Vinod Kumar, S. Hutzler, J. Banhart, Analysis of liquid metal foams through X-ray radioscopy and microgravity experiments, Soft Matter 10 (2014) 6955-6962.

[41]   O. Brunke, A. Hamann, S. J. Cox, S. Odenbach, Experimental and numerical analysis of the drainage of aluminium foams, J. Phys. Condens. Matter 17 (2005) 6353-6362.

[42]   A. Britan, M. Liverts, G. Ben-Dor, S. A. Koehler, N. Bennani, The effect of fine particles on the drainage and coarsening of foam, Colloids Surf., A 344 (2009) 15-23.

[43]   F. Garcia-Moreno, M. Mukherjee, C. Jiménez, J. Banhart, X-ray radioscopy of liquid metal foams under microgravity, Trans. Indian Inst. Met. 62 (2009) 451-454.

[44]   F. Garcia-Moreno, N. Babcsan, J. Banhart, X-ray radioscopy of liquid metalfoams: influence of heating profile, atmosphere and pressure, Colloids Surf., A 263 (2005) 290-294.

[45]   T. Neu, B. Pfretzschner, F. García-Moreno, J. Banhart, Influence of the heating rate on the foaming behavior of various Aluminium alloys, Metals 7 (2017) 323.

[46]   F. Garcia-Moreno, A. Rack, L. Helfen, T. Baumbach, S. Zabler, N. Babcsan, J. Banhart, T. Martin, C. Ponchut, M. Di Michiel, Fast processes in liquid metal foams investigated by high-speed synchrotron x-ray microradioscopy, Appl. Phys. Lett. 92 (2008) 3.

[47]   F. Garcia-Moreno, C. Jiménez, M. Mukherjee, P. Holm, J. Weise, J. Banhart, Experiments on metallic foams under gravity and microgravity, Colloids Surf., A 344 (2009) 101-106.

[48]   T. Ohgaki, H. Toda, M. Kobayashi, K. Uesugi, T. Kobayashi, M. Niinomi, T. Akahori, K. Makii, Y. Aruga, In-situ high-resolution X-ray CT observation of compressive and damage behaviour of aluminium foams by local tomography technique, Adv. Eng. Mater. 8 (2006) 473-475.

[49]   T. Ohgaki, H. Toda, M. Kobayashi, K. Uesugi, M. Niinomi, T. Akahori, T. Kobayash, K. Makii, Y. Aruga, In situ observations of compressive behaviour of aluminium foams by local tomography using high-resolution X-rays, Philos. Mag. 86 (2006) 4417-4438.

[50]   M. Mukherjee, F. García-Moreno, C. Jiménez, A. Rack, J. Banhart, Microporosity in aluminium foams, Acta Mater. 131 (2017) 156-168.

[51]   P. H. Kamm, F. García-Moreno, T. R. Neu, K. Heim, R. Mokso, J. Banhart, Fast synchrotron X-ray tomography of dynamic processes in liquid Aluminium alloy foam Adv. Eng. Mater. 19 (2017) 1600550-n/a.

[52]   F. Garcia-Moreno, M. Mukherjee, C. Jiménez, A. Rack, J. Banhart, Metal foaming investigated by X-ray radioscopy, Metals 2 (2011) 10-21.

[53]   D. J. Durian, Bubble-scale model of foam mechanics: Melting, nonlinear behavior, and avalanches, Phys. Rev. E 55 (1997) 1739-1751.

[54]   N. Vandewalle, J. F. Lentz, S. Dorbolo, F. Brisbois, Avalanches of popping bubbles in collapsing foams, Phys. Rev. Lett. 86 (2001) 179-182.

[55]   M. Paeplow, F. García-Moreno, A. Meagher, A. Rack, J. Banhart, Coalescence avalanches in liquid Aluminum foams, Metals 7 (2017) 298.

[56]   O. Brunke, S. Odenbach, In situ observation and numerical calculations of the evolution of metallic foams, J. Phys. Condens. Matter 18 (2006) 6493-6506.

[57]   F. García-Moreno, L. A. Radtke, T. R. Neu, P. H. Kamm, M. Klaus, C. M. Schlepütz, J. Banhart, The influence of alloy composition and liquid phase on foaming of Al–Si–Mg alloys, Metals 10 (2020) 189.

[58]   E. K. Sichel, R. E. Miller, M. S. Abrahams, C. J. Buiocchi, Heat capacity and thermal conductivity of hexagonal pyrolytic boron nitride, Physical Review B 13 (1976) 4607-4611.

[59]   E. Solórzano, J. A. Reglero, M. A. Rodríguez-Pérez, D. Lehmhus, M. Wichmann, J. A. de Saja, An experimental study on the thermal conductivity of aluminium foams by using the transient plane source method, Int. J. Heat Mass Transfer 51 (2008) 6259-6267.

[60]   C. Jiménez, F. Garcia-Moreno, B. Pfretzschner, M. Klaus, M. Wollgarten, I. Zizak, G. Schumacher, M. Tovar, J. Banhart, Decomposition of TiH_2 studied in situ by synchrotron X-ray and neutron diffraction, Acta Mater. 59 (2011) 6318-6330.

[61]   A. T. Dinsdale, P. N. Quested, The viscosity of aluminium and its alloys--A review of data and models, J. Mater. Sci. 39 (2004) 7221-7228.

[62]   K. Heim, G. S. V. Kumar, F. Garcia-Moreno, J. Banhart, Role of ambient oxygen in the stabilisation of single aluminium alloy films, Procedia Mater. Sci. 4 (2014) 263-268.

[63]   M. Mukherjee, F. Garcia-Moreno, J. Banhart, Defect generation during solidification of aluminium foams, Scripta Mater. 63 (2010) 235-238.

[64]   F. Garcia-Moreno, P. H. Kamm, T. R. Neu, J. Banhart, Time-resolved in situ tomography for the analysis of evolving metal-foam granulates, J. Synchrotron Rad. 25 (2018) 1505-1508.

Figures
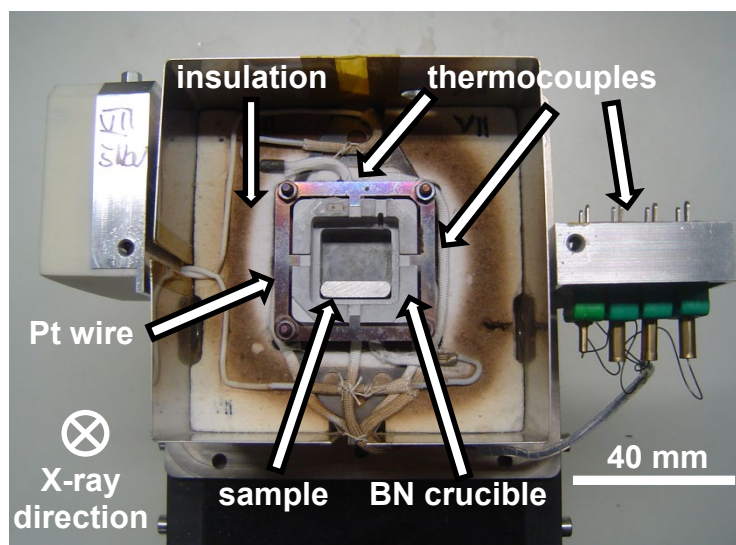
Fig. 1. Foaming furnace with good (± 1 K) spatial temperature homogeneity and temporal stability. A foamable sample is seen at the bottom of the BN crucible.
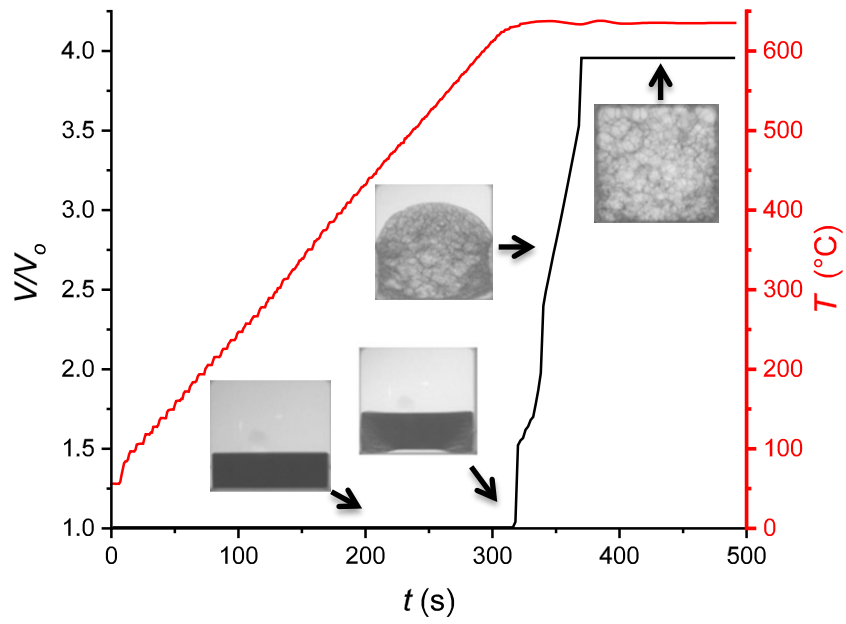
Fig. 2. Heating profile and volume expansion curve of AlSi9 sample. Heating rate is 2 K/s, isothermal holding temperature 635 °C. 4 radiographies extracted from the in-situ radioscopy sequence show the corresponding foam structures at different expansion stages.
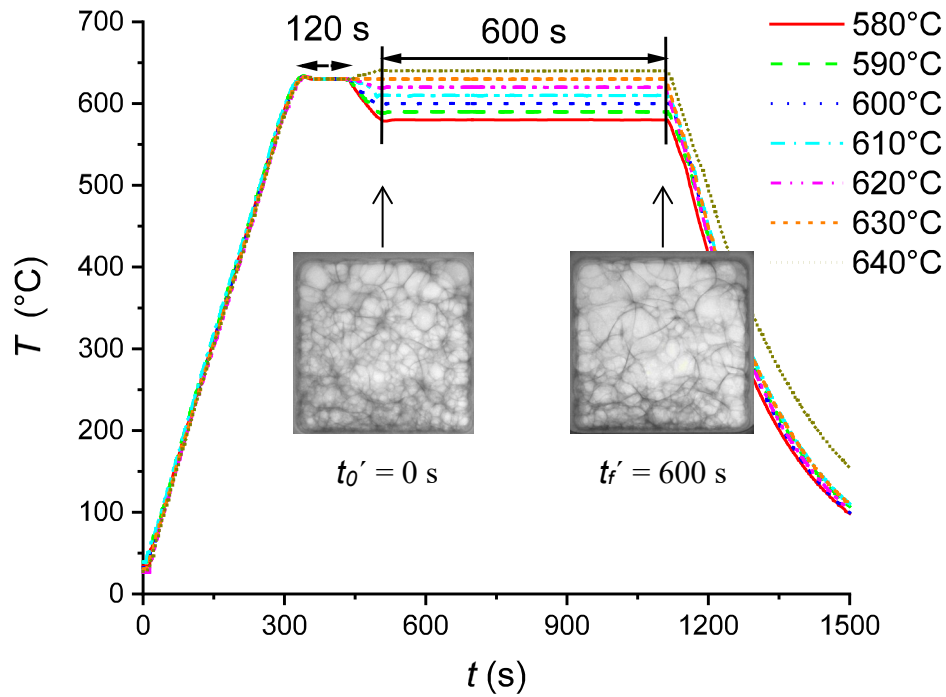
Fig. 3. Temperature profiles applied to AlSi8Mg4 samples with a heating ramp of 2 K/s, a first short isothermal holding step at 630 °C and subsequent 600 s of isothermal holding at varying holding temperatures between 580 °C and 640 °C starting at $t = 500$ s (relative time scale: $t' = 0$ s). The insets show radiographies of the foam structure at the beginning and end of the studied holding period for the experiment conducted at 640 °C.

holding temperature	holding time t'		
	0 s	300 s	600 s
580 °C			
600 °C			
620 °C			
640 °C			

20 mm
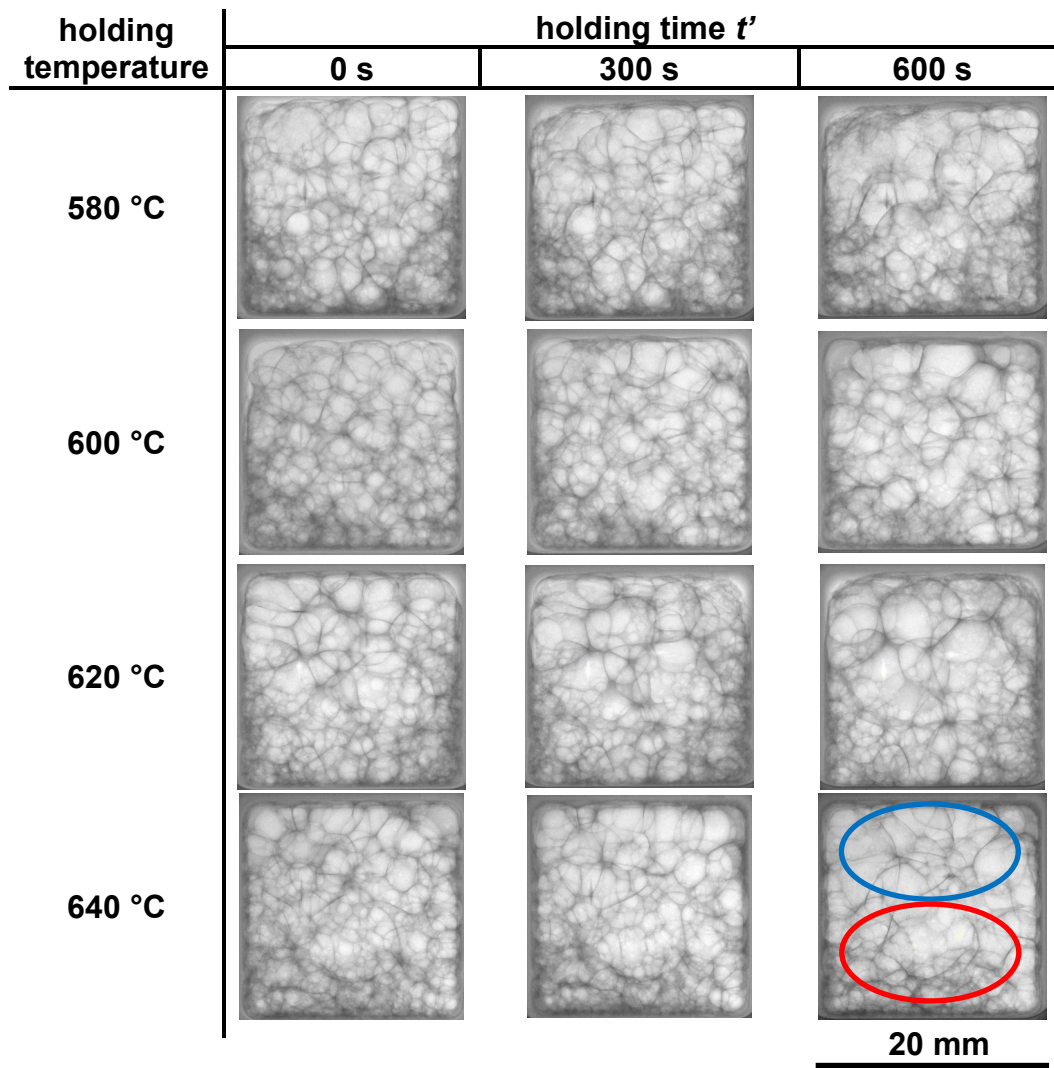
Fig. 4. Representative X-ray radiographies showing how AlSi9 foams evolve during holding at different temperatures. The state before, halfway through and at the end of holding is shown. In one of the images, a blue ellipse marks regions of lower foam density and larger bubbles, a red ellipse denser regions caused by gravity-induced drainage.
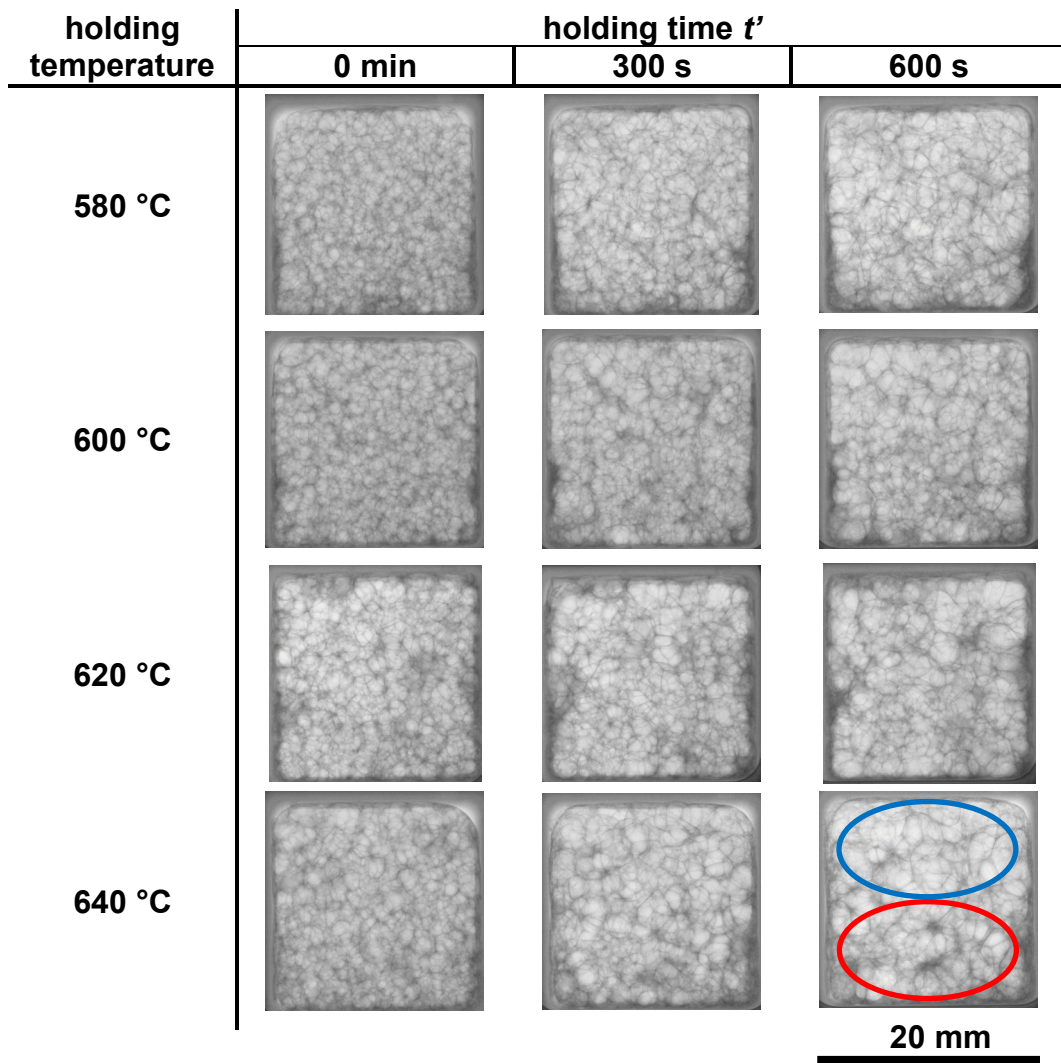
Fig. 5. Same as Fig. 4 for alloy AlSi8Mg4.
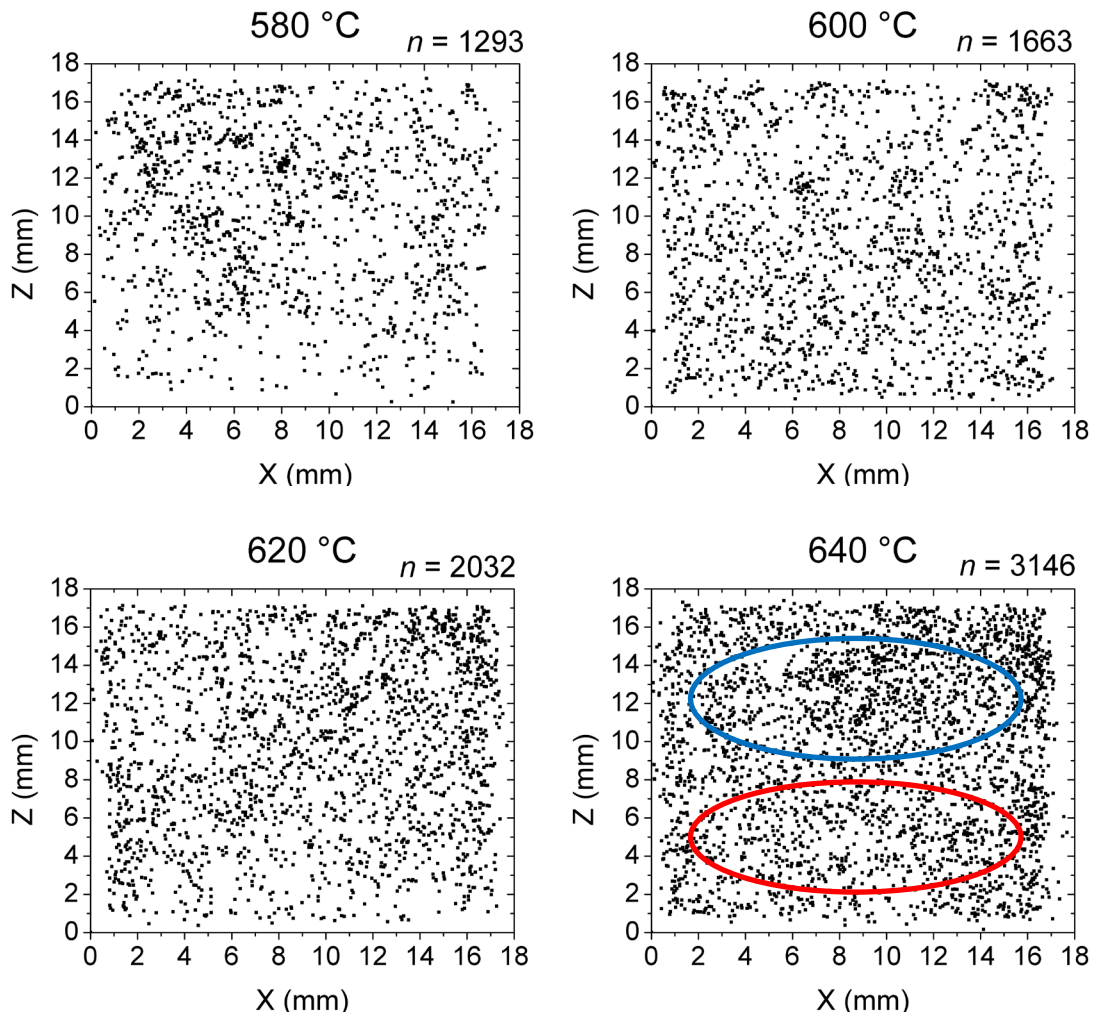
Fig. 6. Spatial distribution of ruptures in AlSi9 foams for different selected holding temperatures. Each dot represents a rupture event. The total number of ruptures n is indicated at the top right of each map. For each temperature, the rupture maps and the total number of ruptures n represent the sum of 5 different individual experiments. A blue ellipse marks regions with more ruptures, a red ellipse regions with fewer ruptures.
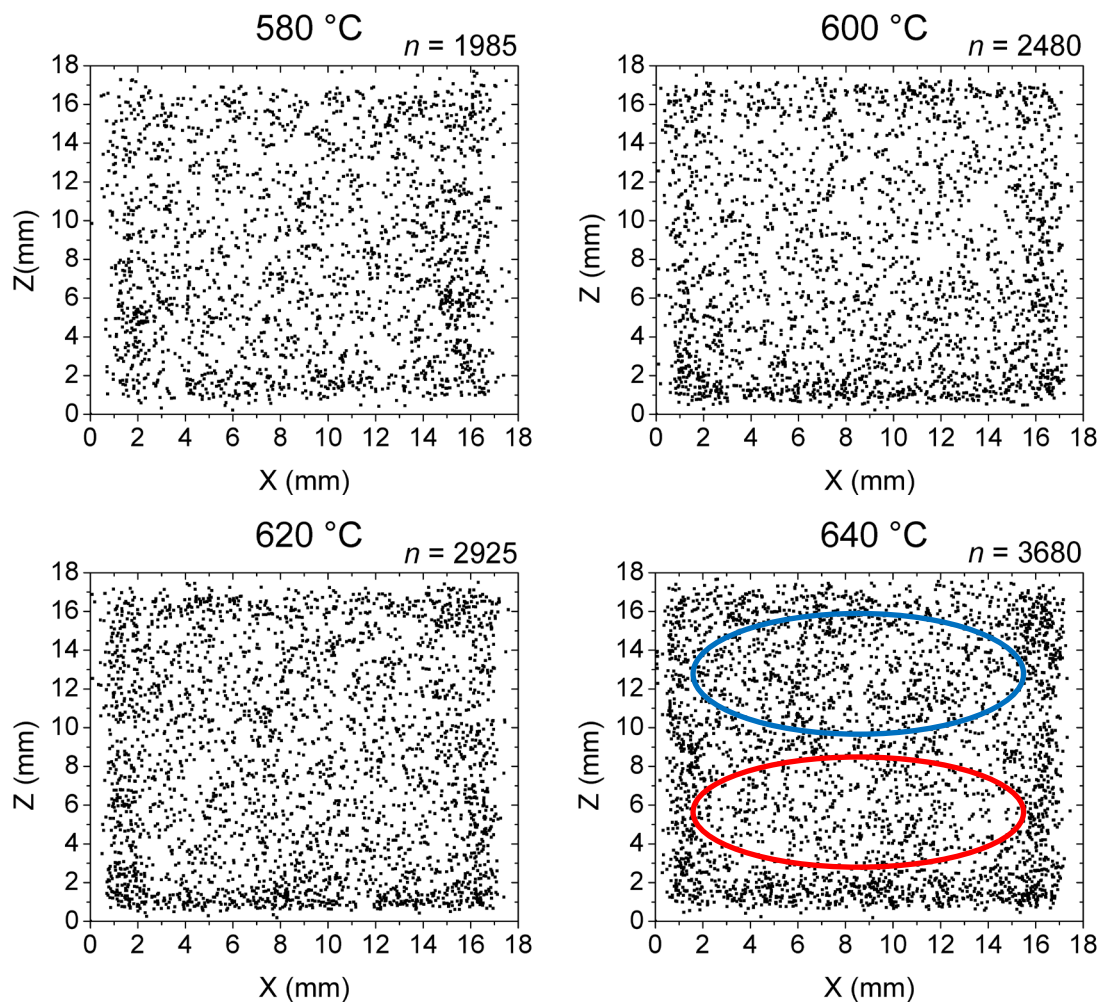
Fig. 7. Same as Fig. 6 for alloy AlSi8Mg4.
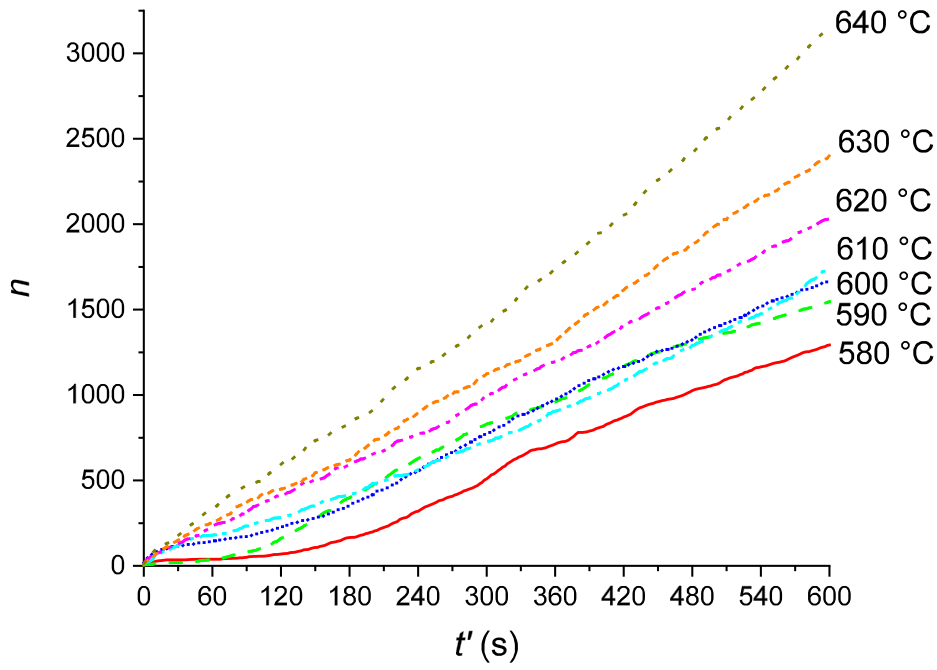
(a)
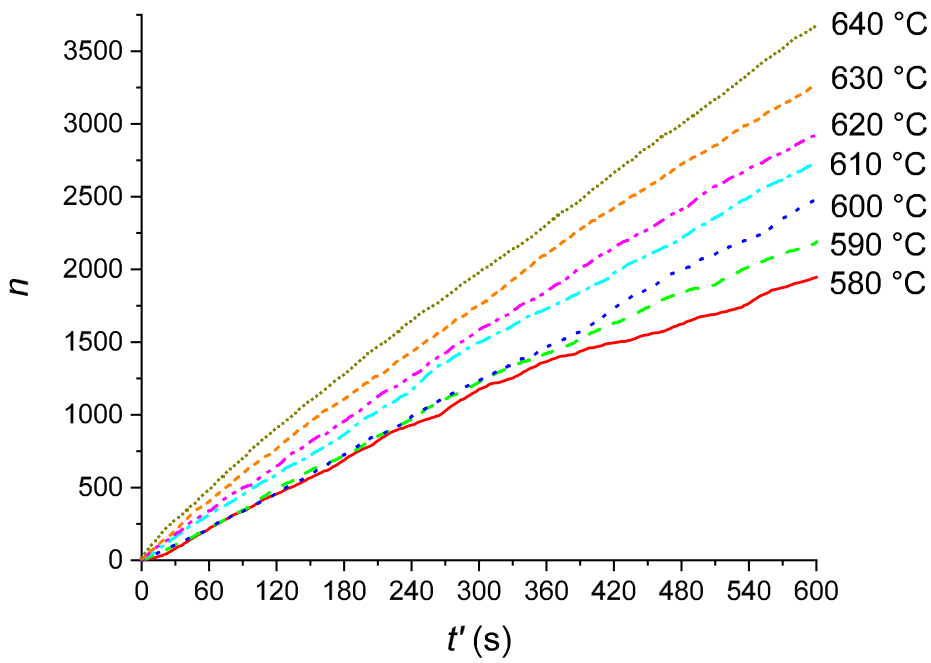
(b)

Fig. 8. Accumulated number of ruptures in the entire foam volume summed up over 5 single experiments for each condition as a function of holding time and for different temperatures. (a) AlSi9 and (b) AlSi8Mg4.
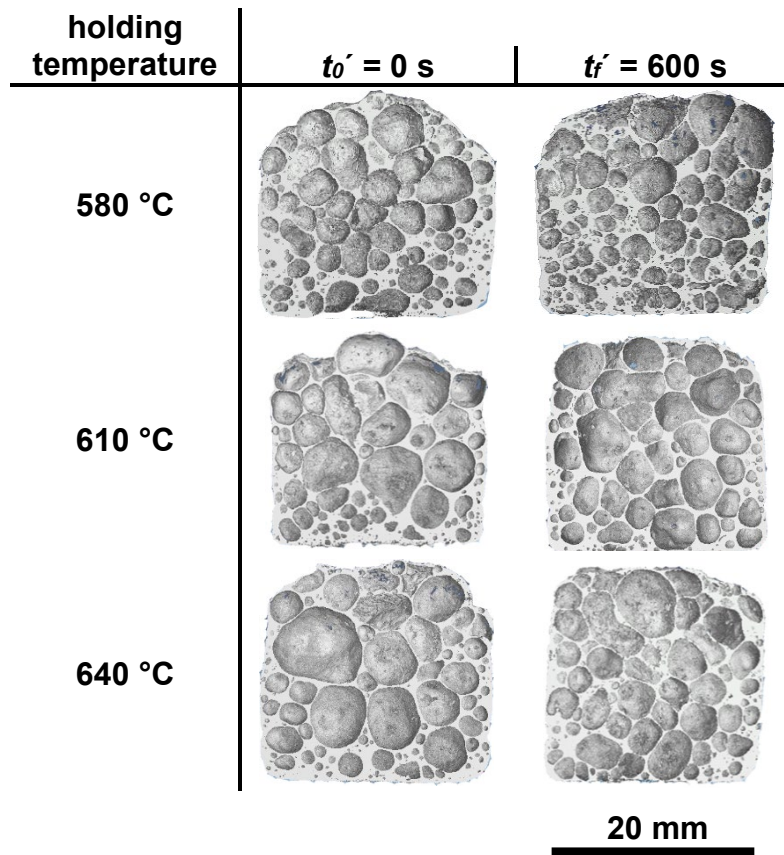
Fig. 9. Cross-sections extracted from tomographies of AlSi9 solid foams solidified at the beginning (t_0') and end (t_f') of isothermal holding.
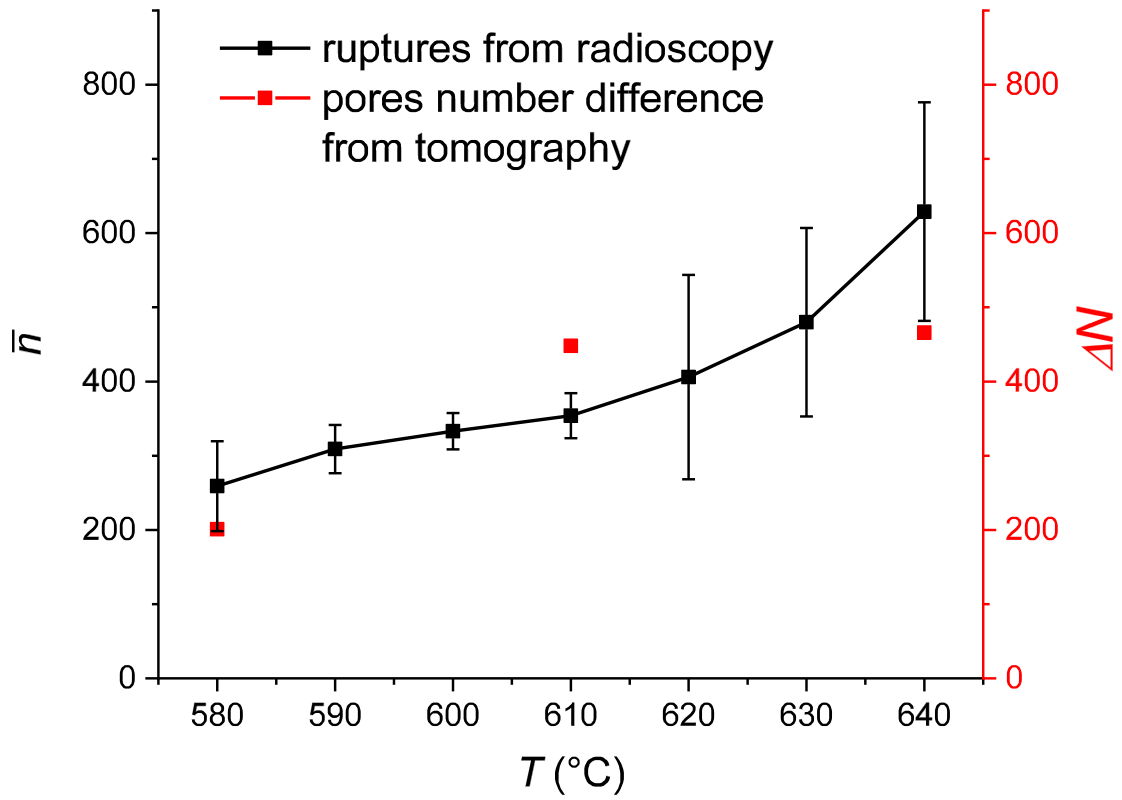
Fig. 10. Comparison of the number of ruptures after holding time t_f' measured by radioscopy (last point in Fig. 8 divided by 5 to express an average sample) and difference of number of pores ΔN as obtained by tomography and applying Eq.(1) for 3 different temperatures.
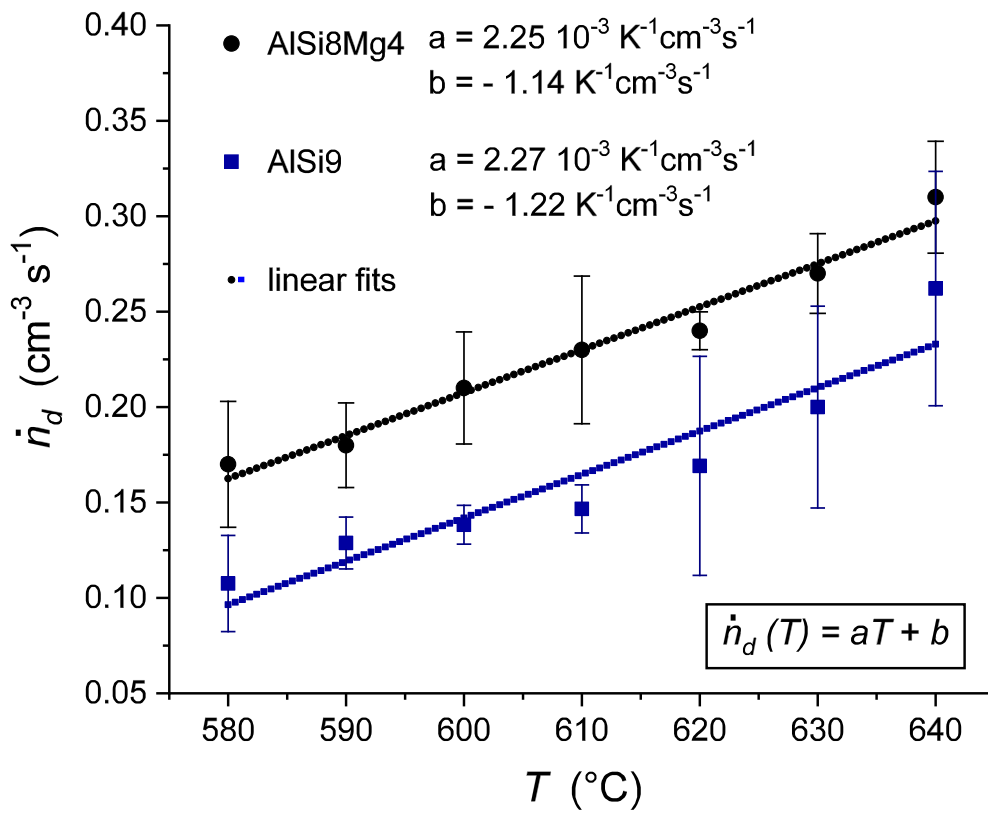
Fig. 11. Film rupture density rate in AlSi9 and AlSi8Mg4 foam averaged over the entire holding period of 600 s and over all the 5 samples foamed at each holding temperature.
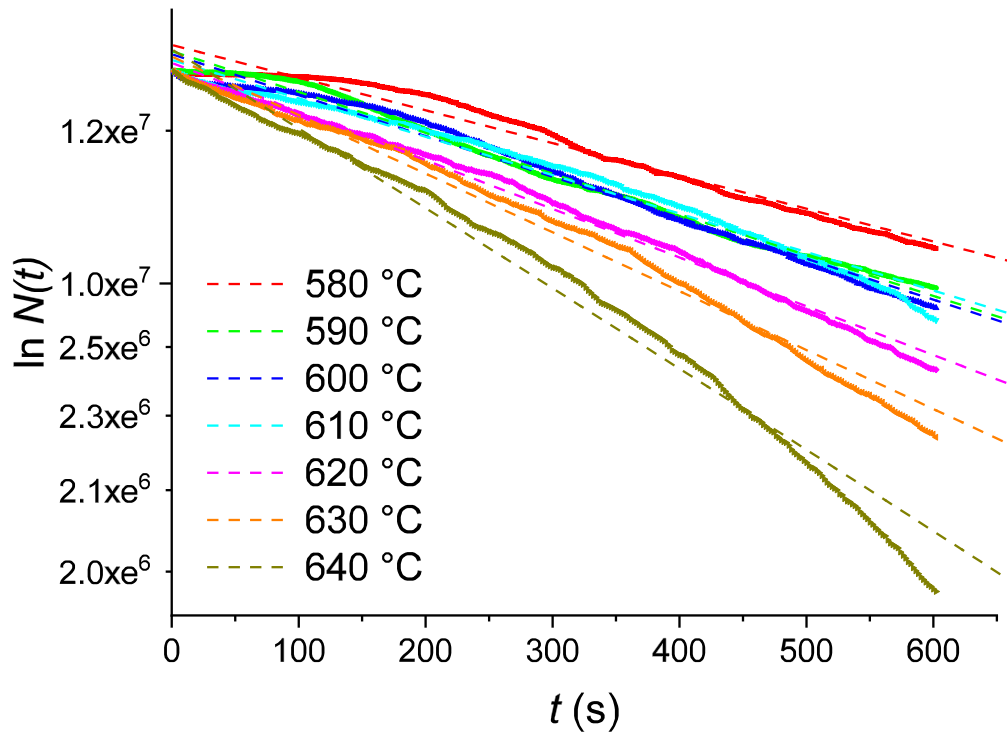
(a)
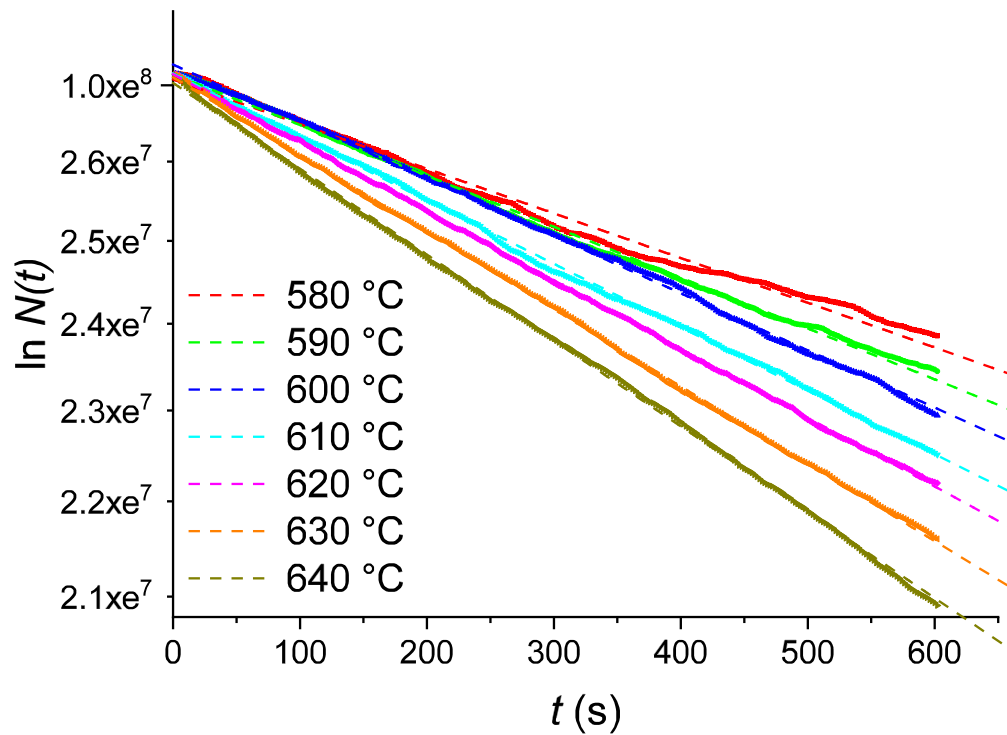
(b)

Fig. 12. Time evolution of the number of bubbles and fitted exponential decay (dashed lines) corresponding to the coalescence theory for (a) AlSi9 and (b) AlSi8Mg4 for different temperatures.
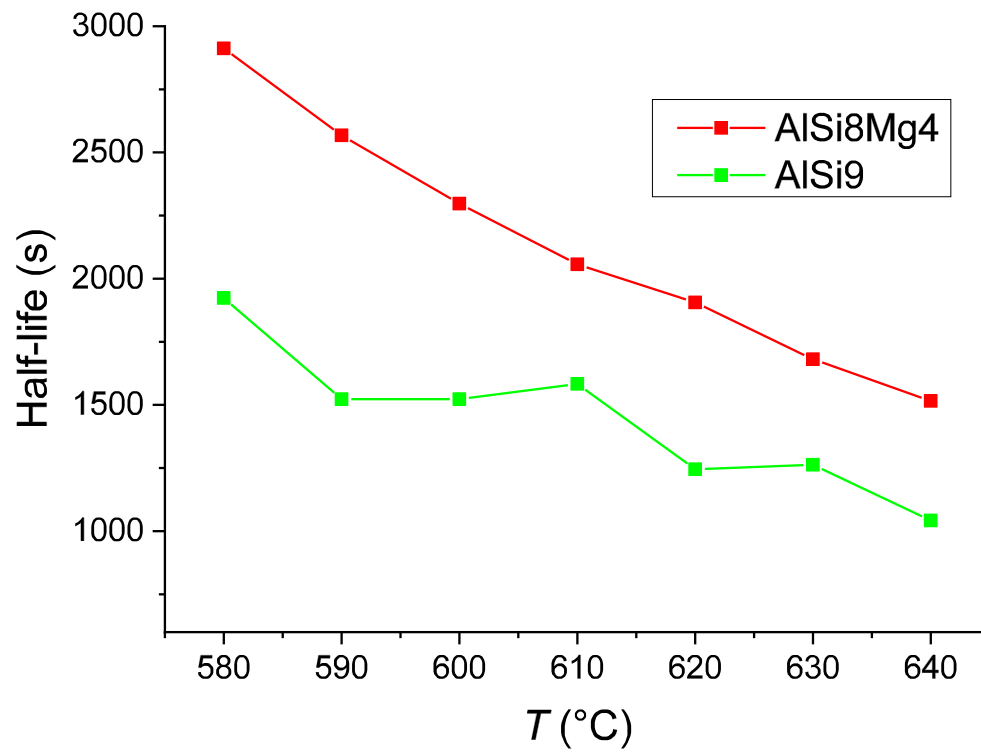
Fig. 13. Half-life of foam in dependence of holding temperature for AlSi9 and AlSi8Mg4.

Tab. 1. Mean number of ruptures $\bar{n}$ and internal stability of AlSi9 and AlSi8Mg4 foams for different holding temperatures.

T (°C)	$\bar{n}_{AlSi9}$	$\bar{n}_{AlSi8Mg4}$	$S_{int,AlSi9}$ (s)	$S_{int,AlSi8Mg4}$ (s)	$S_{int,AlSi8Mg4}/S_{int,AlSi9}$ (%)
580	258±27	397±32	5.42	7.54	139.1
590	309±15	440±25	4.54	6.81	150
600	334±14	496±32	4.21	6.04	143.5
610	349±17	548±42	3.96	5.47	138.1
620	406±62	585±11	3.45	5.12	148.4
630	480±57	655±23	2.92	4.57	156.5
640	629±66	736±31	2.27	4.07	179.3

$$\frac{\bar{S}_{int,AlSi8Mg4}}{\bar{S}_{int,AlSi9}} * 100\% \; = \; 150.7 \pm 5.4\%$$